

Calibration model of a dual gain flat panel detector for 2D and 3D x-ray imaging

C. Schmidgunst^{a)}

Siemens AG, Medical Solutions, Special System Division, Allee am Roethelheimpark 2, 91052 Erlangen, Germany and University of Regensburg, Institute for Bio-Physics and Bio-Chemistry, Computational Intelligence and Machine Learning Group, Universitätsstraße 31, 93040 Regensburg, Germany

D. Ritter

Siemens AG, Medical Solutions, Special System Division, Allee am Roethelheimpark 2, 91052 Erlangen, Germany

E. Lang

University of Regensburg, Institute for Bio-Physics and Bio-Chemistry, Computational Intelligence and Machine Learning Group, Universitätsstraße 31, 93040 Regensburg, Germany

(Received 15 February 2007; revised 19 June 2007; accepted for publication 26 June 2007; published 24 August 2007)

The continuing research and further development in flat panel detector technology have led to its integration into more and more medical x-ray systems for two-dimensional (2D) and three-dimensional (3D) imaging, such as fixed or mobile *C* arms. Besides the obvious advantages of flat panel detectors, like the slim design and the resulting optimum accessibility to the patient, their success is primarily a product of the image quality that can be achieved. The benefits in the physical and performance-related features as opposed to conventional image intensifier systems, (e.g., distortion-free reproduction of imaging information or almost linear signal response over a large dynamic range) can be fully exploited, however, only if the raw detector images are correctly calibrated and postprocessed. Previous procedures for processing raw data contain idealizations that, in the real world, lead to artifacts or losses in image quality. Thus, for example, temperature dependencies or changes in beam geometry, as can occur with mobile *C* arm systems, have not been taken into account up to this time. Additionally, adverse characteristics such as image lag or aging effects have to be compensated to attain the best possible image quality. In this article a procedure is presented that takes into account the important dependencies of the individual pixel sensitivity of flat panel detectors used in 2D or 3D imaging and simultaneously minimizes the work required for an extensive recalibration. It is suitable for conventional detectors with only one gain mode as well as for the detectors specially developed for 3D imaging with dual gain read-out technology. © 2007 American Association of Physicists in Medicine. [DOI: [10.1118/1.2760024](https://doi.org/10.1118/1.2760024)]

Key words: flat panel detector (FD), FD conditioning, FD calibration, dual dynamic range, cone beam CT, lag

I. INTRODUCTION

In medical x-ray imaging the conventional image intensifiers are being replaced step by step by digital flat panel (FD) technology. For example, there are FD-based x-ray systems for mammography or stationary *C* arm systems for angiography and cardiology. Besides already commercially available products, there are several preclinical studies with mobile or stationary prototype systems equipped with FD.¹⁻⁸

Not only obvious advantages on the basis of the geometric properties such as compact design, large field of view (e.g., $40 \times 30 \text{ cm}^2$,^{1,4,9} and the resulting excellent patient access have led to this development but also the physical properties. Among the latter are extended dynamic range (up to 17 bit^{10,11}) high speed (60 fps) and low-noise readout electronics, independence of the terrestrial magnetic field and a long life cycle with respect to inherent radiation damage.

However, the variable properties (offset, gain, lag¹²⁻¹⁴) for each pixel of the detector matrix caused by the panel design

(combination of photodiode, thin film transistor, line/column driver, amplifier, sample and hold unit, A/D converter) have to be corrected for every single detector mode (e.g., field of view, binning, frame rate) to bring out the best in image quality.

For *C*-arm-based systems the quality of the calibration and correction process also depends on beam quality and beam geometry. Due to their weight optimized design the mechanical stability (e.g., suspension and rigidity of the *C* arm) is not as good as the gantry design of a CT system comparatively. As a consequence distortion or deformation are very likely for different *C* arm positions and result in a shift of the illumination.

Especially for mobile systems, an active cooling or tempering of the detector panel is not practicable because the additional weight of the cooling components would conflict with the requirement of maximum possible mobility. In combination with frequent on and off switching, e.g., during

transport from one room to another or after unsteady storage duration, a wide range of operating temperatures of the FD device is possible. Considering the thermal properties of semiconductors (scintillator and photodiode) this results in a temperature dependent sensitivity of each individual pixel.

Both additional effects described above cannot be sufficiently compensated with the conventional method of offset/gain correction^{15,16} for a certain pixel (u,v) of a two-dimensional (2D) image with height u_0 and width v_0 :

$$C(u,v) = \langle \bar{G} \rangle \cdot \frac{R(u,v) - \bar{O}_R(u,v)}{\bar{G}(u,v) - \bar{O}_G(u,v)}, \quad (1)$$

where C represents the corrected image, R the raw image (the FD image without any corrections), \bar{G} the (time) averaged gain image, \bar{O}_R the (time) averaged offset images corresponding to the raw image, \bar{O}_G the (time) averaged offset images corresponding to the gain image. The scalar value $\langle \bar{G} \rangle$ denotes the (spatial) averaged mean (or global mean) of \bar{G} . \bar{G} is also called the gain map, while \bar{O}_G/\bar{O}_R are called offset maps.

In 1998, Seibert *et al.*¹⁶ proposed a different method for flat-field calibration. Several averaged gain images were taken at different dose levels, starting from very low dose to saturation. A pixel by pixel linear interpolation in sections reduces stripe artifacts due to nonlinear exposure response.

In 2006 this approach was further improved by using the appropriate polynomial instead of a linear fit (Kwan *et al.*¹⁷). It provides excellent correction throughout the entire exposure range, but it does not yet consider the effects caused by temperature dependencies of the semiconductor materials and possible distortion and deformation by detector movement, as for example, during rotation of the C arms.

In 2004, the dual gain mode was presented by Colbeth *et al.*¹¹ It provides a higher dynamic range and better signal-to-noise ratio (SNR) within the important part of the image histogram at the same time. But, on the other hand, it increases the effort for a sufficient flat-field calibration, which is very important in terms of cone beam computer tomography (CBCT). A calibration method for the dual gain mode was introduced by Matistinos *et al.*¹⁰ in 2006, but it also disregards the above-mentioned aspects.

For image sequences also, the lag effect of flat panel detectors as described by Siewerdsen *et al.*^{12,13} influences the quality of the calibration and, therefore, has to be taken into consideration as well. The additional effects determined by detector aging as e.g., loss in sensitivity result in invalid calibration maps and require extensive recalibration.

In this article a calibration model for a dual gain flat panel detector is described, which considers all relevant effects and dependencies that can occur at CBCT with mobile C arm systems, and which simultaneously minimizes recalibration efforts:



FIG. 1. C arm prototype with flat panel detector for cone beam CT imaging.

- For the first time temperature dependencies of the flat panel are considered and integrated in the calibration and correction process without the need for any temperature sensors.
- The effects of the variation of the beam geometry, which are very likely for cone beam CT with mobile C arm and influence image quality (2D/3D), as well as effects of detector aging are taken into account and compensated.
- The idea of multipoint gain calibration, which compensates nonlinear signal response, is enhanced and adapted to dual gain readout mode (DGR) for the first time
- A correction algorithm for the lag effect, which can cause shadow images within image sequences (e.g., at object or system movement), was integrated in the calibration and correction model.

All the steps of the new calibration and correction model are described in detail and the impact of each step is illustrated. Finally, the improvement regarding image quality is demonstrated on phantom studies. The benefit for clinical applications is currently evaluated within the scope of a multicentric study.

II. MATERIAL AND METHODS

II.A. Basic system

All studies have been performed with a specially developed prototypical system for 3D imaging.¹ It is based on a commercial mobile isocentric C arm device (Powermobil, Siemens Medical Solutions) with an additional motor control to provide an automatic and highly reproducible orbital rotation of nearly 180° (see Fig. 1). It should be noted that for CBCT a rotation angle of 180° plus beam angle is theoretically necessary to provide a minimal complete dataset for 3D reconstruction. That is why uncorrectable artifacts due to undersampling will persist in the reconstructed volume. For a CBCT scan, up to several hundred projection images are acquired in equidistant angles during a 180° orbital rotation. The number of images depends on the designated 3D image quality (bone or soft tissue resolution).

As the average power of the mobile x-ray generator is restricted by the provision of electricity, there are basic limi-

tations to pulse rate, pulse shape, and x-ray window. The requirement for reproducibility of scan geometry and mechanical limitations constrict the maximal rotation speed. Therefore, a frame rate of 6.2 fps is practical for this prototype system, which is compatible with a scan time of 32 s and 200 projection images during 180° rotation. However, most scans are done with half this rotation speed (3.1 fps) to guarantee a stable synchronization of detector and x-ray tube.

As soft tissue resolution within the 3D volume is the focus of the studies, a typical voltage of 100 kV is used. For lower kV settings the penetrability of the x-ray photons is less, so that photons at the lower end of the spectrum are strongly absorbed by the object. This changes the beam quality and can cause beam hardening artifacts, because the detector sensitivity is also energy dependent.

II.B. Flat panel detector (FD)

In this study a FD for CBCT is used for the x-ray conversion (PaxScan 4030CB, Varian Inc.⁹). This FD uses an indirect method of detection. Generation of the digital signal is done in two steps. In a first step x-ray photons are absorbed in a scintillator layer (CsI:TI). Their energy is converted to emit amplified photon intensity. Second, these optical photons are detected by amorphous silicon (a-Si) photodiodes arranged on arrays to form the image matrix.

The active matrix size of the panel is 40 × 30 cm². With a pixel pitch of 194 μm this corresponds to a resolution of 2048 × 1536 pixels in unbinned overview modes. Due to the split readout design, that is the upper and lower halves of the detector dispose of their own readout electronics, a parallel readout of both halves is possible. Therefore a theoretical readout rate of 15 fps could be achieved for the overview mode. With binning, even higher frame rates are possible.

The FD is not actively cooled, which means that heat dissipation is done only by heat emission. With a nominal power consumption of 50 W and an external additional x-ray shielding, this can result in possible chassis temperatures of up to 50 °C. Therefore, temperature effects of the semiconductor materials have to be accounted for within a wide range from 15 °C to 50 °C (see Sec. II E 3). Waiting for the steady-state temperature (approximately after 4 h) might not be possible in practice for mobile C arms because a changing of the location (e.g., operation room to emergency room) and frequent unplugging cause temperature variations of the detector.

II.C. Dual gain readout (DGR)

As a unique feature, this FD provides a special gain mode for CBCT applications called dual gain readout mode.^{10,11} A standard high gain mode (see Table I) offers a maximum number of gray levels for the important part of an image (high attenuation areas of the irradiated object, see Fig. 2). But on the other hand, its dynamic range is limited by the small storage capacity (0.5 pF) in the readout circuits. High doses, e.g., necessary for soft tissue resolution, could result in pixel saturation in the direct radiation or low attenuation

TABLE I. Detector modes.^a

Mode	Capacity	Saturation dose	Dimension (width × height)	A/D bit resolution
2 × 2 high gain	0.5 pF	2 μGy	1024 × 768	14
2 × 2 low gain	3.5 pF	15 μGy	1024 × 768	14
2 × 1 high gain	0.5 pF	4 μGy	1024 × 1536	14
2 × 1 low gain	3.5 pF	30 μGy	1024 × 1536	14
DGR = high gain + low gain	0.5/3.5 pF	30 μGy	1024 × 1536 raw image 1024 × 768 combined	2 × 14 raw image (pseudo) 17 combined

^aDefinition: mode characteristic: All additional settings and parameters, such as frame rate, x-ray window, and internal detector configuration are summarized as mode characteristics of the particular mode.

areas (e.g., skin border, thorax) within the image. This information can not be used for 3D reconstruction. It is not critical for the direct radiation area, because it does not contain any information about the object, but it has a major effect if real object information is truncated. The reconstruction of object borders may be partly incomplete and do not represent the real object.

This problem could be minimized by using a low gain mode (see Table I) with a higher storage capacity (3.5 pF). Seven times the dose in comparison to the high gain mode can be detected before the pixels start to saturate. But due to exponential attenuation with the path length, the object information is normally located in the lower part (approximately 10%–15%) of the image histogram (see Fig. 2). The quantization step also increases by a factor of 7, which reduces the number of gray values and increases the quantization noise.

For comparison reasons noise contributions can be expressed by the standard deviation of the gray values (one gray level corresponds to 1 least significant bit) (LSB). The amount of quantization noise (=1.0 LSB,) for the low gain mode is still significantly less than the electronic noise (≈3.8 LSB). Therefore, the maximal contrast resolution is limited by the electronic noise performance of the detector mode.

Despite the seven times higher sensitivity of the high gain mode (0.5 pF versus 3.5 pF) the electronic noise does not increase by this factor. Only ≈4.4 LSB of electronic noise is measured within a dark field image, instead of 3.8 LSB*7 = 26.6 LSB. That is why the high gain mode provides a better SNR than the low gain mode in the electronic noise dominated dose range (see Fig. 2). In the quantum noise dominated dose range the advantage of the high gain mode becomes less important, and both modes should perform similarly. The crossover characteristic from maximal benefit (dark field image, only detector noise) to equalization (white image, very high dose) is fluent and nonlinear.

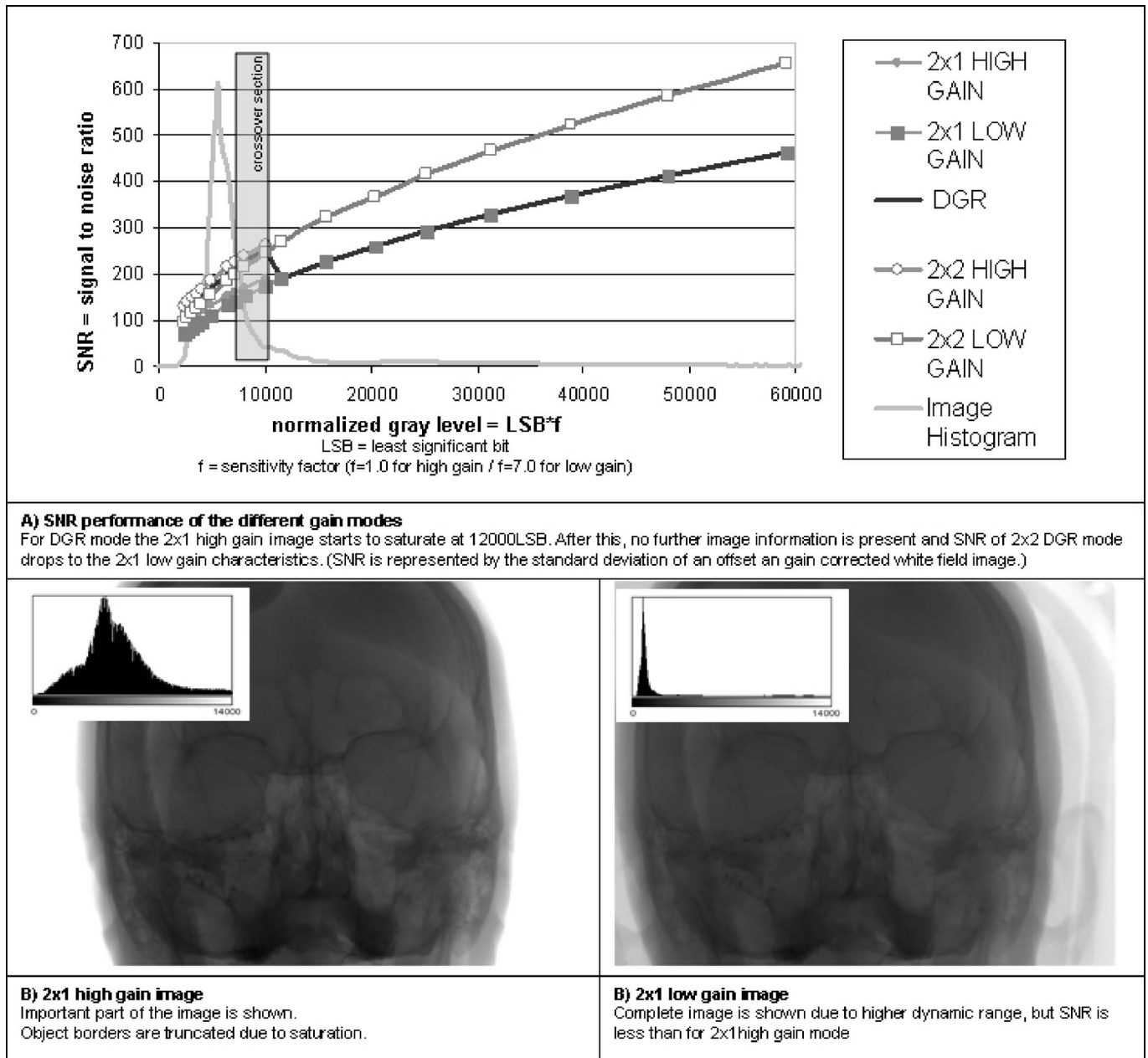


FIG. 2. Signal-to-noise performance of different detector modes.

In order to benefit from relevant advantages of high and low gain the dual gain mode (DGR, see Table I) is introduced. In practice, it is implemented in the following way:

Instead of reading the panel with 2×2 binning in low gain (3.5 pF capacity) or high gain (0.5 pF capacity), lines are read out alternately, which means one line in high gain the next in low gain. Initially, only columns are binned (2×1 binning), so the dimension of the raw image is 1024×1536 pixels. Due to the split design of the detector, a read-out of the two halves of the detector is performed at the same time starting with the outermost lines and proceeding toward the center. If the first lines are read at low gain, the last two lines, in the middle of the image, are high gain lines.

Two images, one low gain and one high gain image with a dimension of 1024×768 pixels, can be separated from the

raw image. As a first step, these images have to be corrected for offset, gain, and additionally for possible defects. Afterwards the low and high gain images with 14 bit dynamic range are fused to one image with increased dynamic range. The high gain image remains unchanged while the low gain image is multiplied by the capacity factor, that is the ratio of the mean value of an offset and gain corrected high gain white field image and the mean value of the corresponding offset and gain corrected low gain white field image. This factor is a global value because the pixel individual sensitivity is compensated after gain correction, meaning each pixel has the same signal response. In practice the capacity factor is approximately 7, which conforms to the ratio of the capacitors for high and low gain. After this scaling the low and high gain images are added together pixel by pixel to obtain

the final image. This image has a pseudodynamic range of 17 bits, that is the maximum signal is $2^{14} \times 7$, which is close to 2^{17} . We call this “pseudo 17 bits” because the quantization step for gray level values greater than 2^{14} is equal to 7 rather than 1.

II.D. Calibration and correction model

Generally the calibration and correction model can be separated into two parts: Offline calibration and online correction. The offline calibration includes all steps necessary to acquire the information that is later used for the online correction of the raw images. The activity diagram for the offline calibration procedure (see Fig. 3) gives a rough overview of the basic action and generated elements (e.g., offset, gain, and delta maps) that are stored in the calibration data pool. During the online correction procedure (see Fig. 4) the elements from the calibration data pool are used to correct the present image or image sequence. The generation and use of each element will be described in detail later.

Because of the dependencies between the different calibration maps and image sequences, a special notation is proposed. Basically there is a differentiation between the calibration maps and image sequences. Maps are represented by capital Greek symbols while image sequences are represented by capital Latin letters. Table II gives an overview of the object types used. For calibration maps of the dual gain mode, an index $X \in \{H, L\}$ is necessary to separate the low and high gain. $X \in \{H, L\}$ is positioned on the upper right of the map symbol. The dependent parameters such as image dose, temperature, or orbital rotation angle are represented by an index on the upper left of the map symbol (see Table III). The lower right index corresponds to the method of statistical computation (e.g., the temporal averaged mean value M , standard deviation SD , spatial averaged global mean value G , see Table IV).

As maps are always single images there is no counting index on the lower right. For example, the pixel individual gain map mean values for the low gain (${}_M\Gamma^L$) at a certain image dose (d), rotation angle (r), and temperature (t) and can be written as

$${}_{d/r/t}\Gamma^L(u, v). \tag{2}$$

For simplicity only the variable environmental parameters are specified, while static parameters are omitted.

As image sequences consist of multiple images, a counting index (s, n) is given in the lower right (s represents the series number, if more than one series is present, n represents the image number of the corresponding series s). For dual gain mode a separation index $X \in \{H, L\}$ in the upper right is necessary, in turn. The parameter on the upper left gives the status of correction (see Table V). A computation index is not necessary. Therefore, a certain high gain image of a certain white field sequence ($W_{s,n}^H$), which is offset (ω), delta (δ), and gain (γ) and corrected, can be written as

$${}^{\omega/\delta/\gamma}W_{s,n}^L(u, v). \tag{3}$$

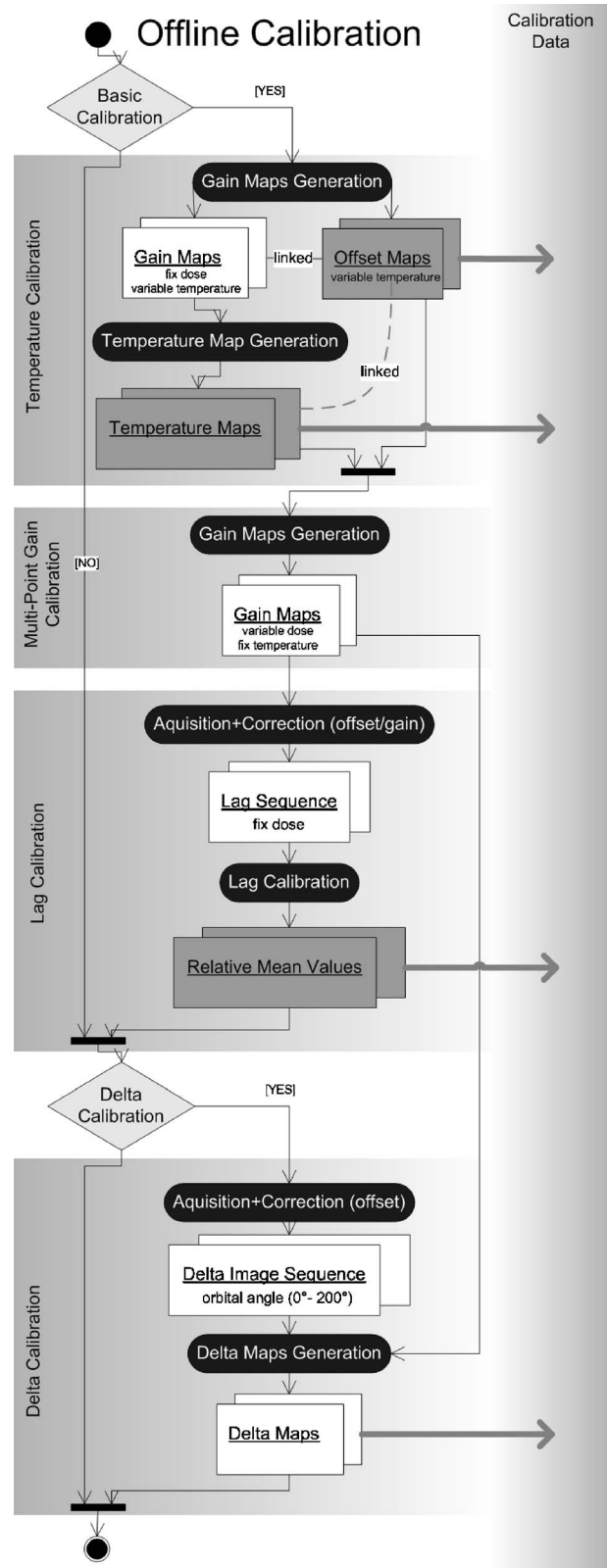


FIG. 3. Activity diagram for offline calibration process.

II.E. Offline calibration

A complete offline calibration is done in four steps (see Fig. 3): The first step is the temperature calibration. It com-

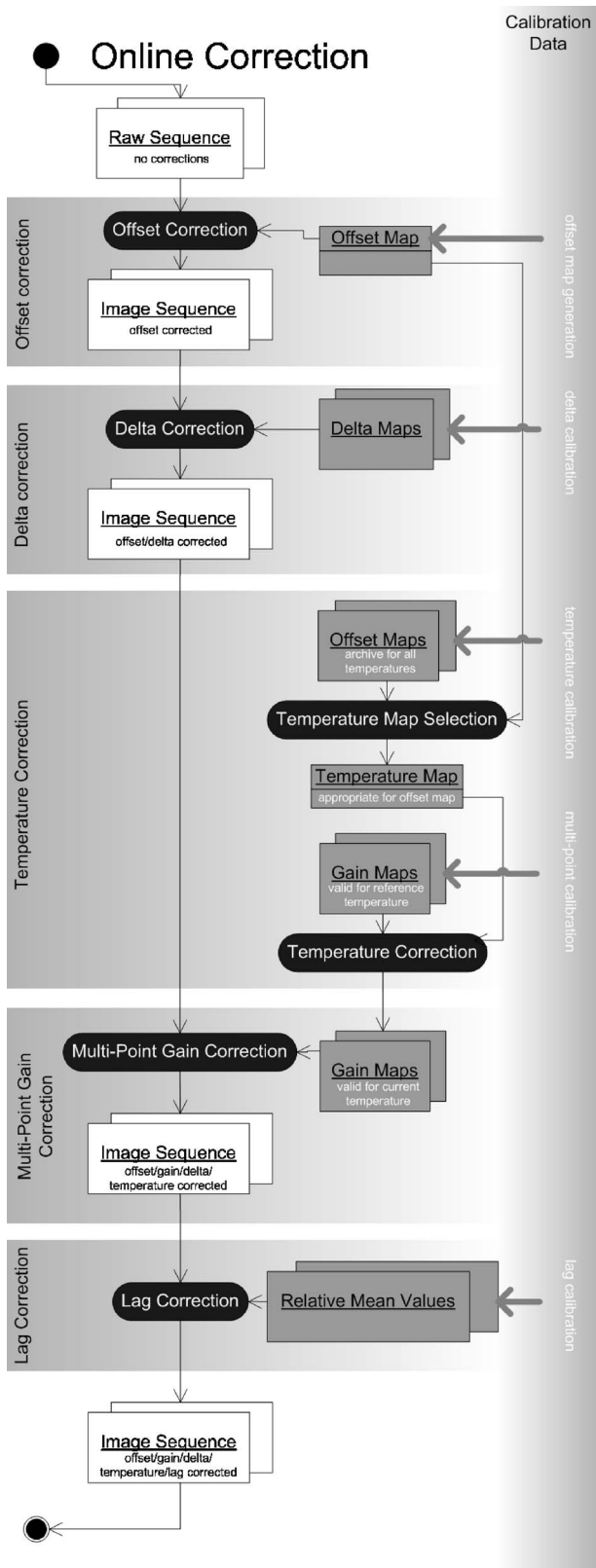


FIG. 4. Activity diagram for online correction process.

compensates temperature effects and dependencies such as the temperature based sensitivity drift of a mobile detector without active cooling during the warm-up period.

TABLE II. Notation for calibration maps (capital Greek letters) and image sequences (capital Latin letters).

Denotation	Symbol	Description
Offset map	Ω	calibration map
Gain map	Γ	calibration map
Delta map	Δ	calibration map
Temperature map	Θ	calibration map
Dark field sequence	D	image sequence without radiation
White field sequence	W	image sequence with radiation, but without any objects
Image sequence	I	regular image sequence

The second step is a multipoint gain calibration for the dual gain mode, which compensates streak or stripe artifacts within the 2D image due to pixel individual nonlinear signal response.

The third step is the lag calibration. The detector specific decay curve (depends on mode characteristic, see Table I) for image lag due to afterglow from the scintillator and signal retention in the panel is measured. Steps one to three are part of the basic calibration, which has to be done only once at initial operation.

As a last step, a delta calibration is performed. It compensates all dynamic effects. Among the latter are variations of the illumination uniformity caused by deformation of the C arm while rotating or modifications of pixel sensitivity due to

TABLE III. Notation for environmental indices (small Latin letters).

Denotation	Symbol	Description
Image dose step	d	index representing current dose settings (see Tab. V)
Temperature	t	index representing current temperature
Rotation angle	r	index representing current orbital angle

TABLE IV. Statistical computation indices (capital Latin letters).

Denotation	Symbol	Description
Mean value	M	(temporal averaged) mean value of pixel (u, v)
Standard deviation	SD	(temporal referable) standard deviation of pixel (u, v)
Global mean value	G	(spatial averaged) mean value of image or map

TABLE V. Correction indices (small Greek letters).

Denotation	Symbol	Description
Offset	ω	indicates offset correction
Gain	γ	indicates gain correction
Delta	δ	indicates delta correction
Temperature	ϑ	indicates temperature correction

detector aging. This step has to be repeated in regular periods to guarantee good compensation performance.

For offline calibration as well as for online correction two basic types of calibration maps are needed: The offset map and gain map. The creation of these maps is described below.

II.E.1. Offset map generation

For offset map generation a dark field image sequence is necessary. A fixed frame rate guarantees constant integration period for the offset of each image. In order to reduce the detector noise up to 100 dark field images D_n^X are acquired at fixed mode characteristic (see Table I) for the DGR mode. Mean map ${}_M\Omega^X$ and standard deviation map ${}_{SD}\Omega^X$ for both gains ($X \in \{H, L\}$) are stored as maps in the offset map set:

$${}_M\Omega^X(u, v) = \frac{1}{N} \cdot \sum_{n=1}^N D_n^X(u, v), \quad (4)$$

$${}_{SD}\Omega^X(u, v) = \sqrt{\frac{1}{N} \sum_{n=1}^N ({}_M\Omega^X(u, v) - D_n^X(u, v))^2}. \quad (5)$$

The standard deviation map will be used for defect pixel detection. Therefore, an offset map set for DGR mode includes four maps with identical dimension (u_0, v_0) composed as $\hat{\Omega}$:

$$\hat{\Omega} = \{{}_M\Omega^H(u, v), {}_M\Omega^L(u, v), {}_{SD}\Omega^H(u, v), {}_{SD}\Omega^L(u, v)\}. \quad (6)$$

II.E.2. Gain map generation

In order to create a gain map a valid or updated offset map $\hat{\Omega}$ is necessary. Up to 100 white field images ${}^dW_n^X$ are acquired at a certain dose step d (see Table V) and tube voltage (e.g., 100 kV). The gain map matrices for both gains ($X \in \{H, L\}$) are computed as follows:

$${}^d_M\Gamma^X(u, v) = \left(\frac{1}{N} \cdot \sum_{n=1}^N {}^dW_n^X(u, v) \right) - {}_M\Omega^X(u, v), \quad (7)$$

$${}^d_{SD}\Gamma^X(u, v) = \sqrt{\frac{1}{N} \sum_{n=1}^N ({}^d_M\Gamma^X(u, v) - {}^dW_n^X(u, v) + {}_M\Omega^X(u, v))^2}. \quad (8)$$

The standard deviation maps for high and low gain will be used for defect pixel detection. The global mean values for high and low gain are computed as follows:

$${}^d_G\Gamma^X = \frac{1}{u_0 v_0} \sum_{u, v} {}^d_M\Gamma^X(u, v). \quad (9)$$

A gain map set for the DGR mode includes four maps with identical dimension (u_0, v_0) plus the global mean values ${}^d_G\Gamma^H, {}^d_G\Gamma^L$ composed as ${}^d\hat{\Gamma}$:

$${}^d\hat{\Gamma} = \left\{ \begin{array}{l} {}^d_M\Gamma^H(u, v), {}^d_M\Gamma^L(u, v), {}^d_{SD}\Gamma^H(u, v), {}^d_{SD}\Gamma^L(u, v) \\ {}^d_G\Gamma^H, {}^d_G\Gamma^L \end{array} \right\}. \quad (10)$$

II.E.3. Calibration step 1: Temperature calibration

For temperature calibration several gain maps at fixed exposure (e.g., dose index $d=6$, which is about 90% of the saturation level of the high gain mode) and their corresponding offset maps are generated during the warmup period. As housing temperatures at the rear side of the detector between room temperature ($t_B \approx 20^\circ\text{C}$) and reference temperature $t_E \approx 50^\circ\text{C}$ can be measured, a step of 2°C is adequate since for temperature variations of less than 1°C no significant differences in the pixel individual sensitivity was observed. This results in 15 offset and gain maps. Pairs of offset and gain maps that were acquired at the same temperature belong together:

$${}^t_M\Gamma^X(u, v) \Leftrightarrow {}^t_M\Omega^X(u, v),$$

$$t \in \{t_B, \dots, t_E\}. \quad (11)$$

The last gain map that was acquired after the warm-up period is selected as reference map. A temperature map ${}^t\Theta^X$ consisting of pixel individual weight factors is computed for each gain map ${}^t_M\Gamma^X$ via a division by the reference gain map ${}^{t_E}_M\Gamma^X$:

$${}^t\Theta^X(u, v) = \frac{{}^t_M\Gamma^X(u, v)}{{}^{t_E}_M\Gamma^X(u, v)} \Leftrightarrow {}^t_M\Omega^X(u, v). \quad (12)$$

These temperature maps ${}^t\Theta^X$ are also linked to the corresponding offset maps ${}^t_M\Omega^X$ that were acquired at the same temperature. It should be noted that only the temperature maps build the dataset for further temperature correction.

II.E.4. Calibration step 2: Multipoint gain calibration

For multipoint gain calibration several gain maps at fixed temperature (e.g., after the warm-up period) are acquired at different dose settings (kV constant, mAs variable). The number of maps and their distribution along the dynamic range depend on the level of nonlinearity of the signal response and the expected dose behind the interesting object (system dose). More steps near system dose are recommended. Within the nearly linear range only a few steps are necessary, within the nonlinear range gaps between two dose settings have to become smaller. For the DGR mode, the distribution shown in Table VI appeared practical. It should be noted, that the number and distribution of the dose steps can be further optimized to reduce the data volume and calibration effort on the one hand, but to preserve the image quality on the other hand. Finding the best possible configuration is focus of present studies.

Accordingly, a complete dataset for a multipoint gain calibration consists of 14 gain maps or 56 matrices of identical dimension at the specified dose settings d :

$${}^d\hat{\Gamma} d = 1, \dots, 14. \quad (13)$$

Saturated high gain maps are not used for calibration but for the detection of a special class of defect pixel (see Sec. II F 6). Theoretically, only one saturated gain map of the high gain is necessary for that purpose (e.g., $d=9$).

TABLE VI. Calibration step index/dose parameter..

Calibration step index d	Average tube current (mA)	Charge/image (mAS)	High gain saturation (%)	Low gain saturation (%)
1	0.1	0.05	18.9	2.5
2	0.2	0.10	24.5	3.2
3	0.3	0.15	34.8	4.6
4	0.4	0.20	43.7	5.8
5	0.5	0.25	64.6	8.5
6	0.6	0.30	93.4	12.2
7	0.9	0.45	—	16.6
8	1.2	0.60	—	21.2
9	1.5	0.75	—	26.8
10	1.8	0.90	—	33.4
11	2.3	1.15	—	41.3
12	2.9	1.45	—	51.1
13	3.7	1.85	—	63.8
14	4.6	2.30	—	85.6

II.E.5. Calibration step 3: Lag calibration

In order to compensate ghosting or lag effects^{12,13} within an image sequence, the composite decay curve of afterglow in the scintillator (CsI:TI) and signal retention in the panel has to be determined. This decay behavior was measured to be the same for each pixel, within the accuracy of the measurement (5%), so no pixel individual correction is necessary.

For calibration an offset and gain corrected image sequence $\omega/\gamma I_n(u,v)$ with only one exposed image ($n=0$) at fixed mode characteristic is necessary. To increase SNR, a relatively high dose setting within the linear signal response range (e.g., $d=10$) is chosen. The global mean values $\omega/\gamma I_n$ are measured for the initial image $n=0$ and all subsequent images ($n=1, \dots, N$). It should be noted that the global mean values $\omega/\gamma I_n$ do not represent the designated decay curve. But the latter can be reconstructed with this information (see Fig. 5). All images whose global mean value falls below the offset noise level are clipped (only $N_0 < N$ images remain for further computation). The absolute lag value L^{abs} (represent-

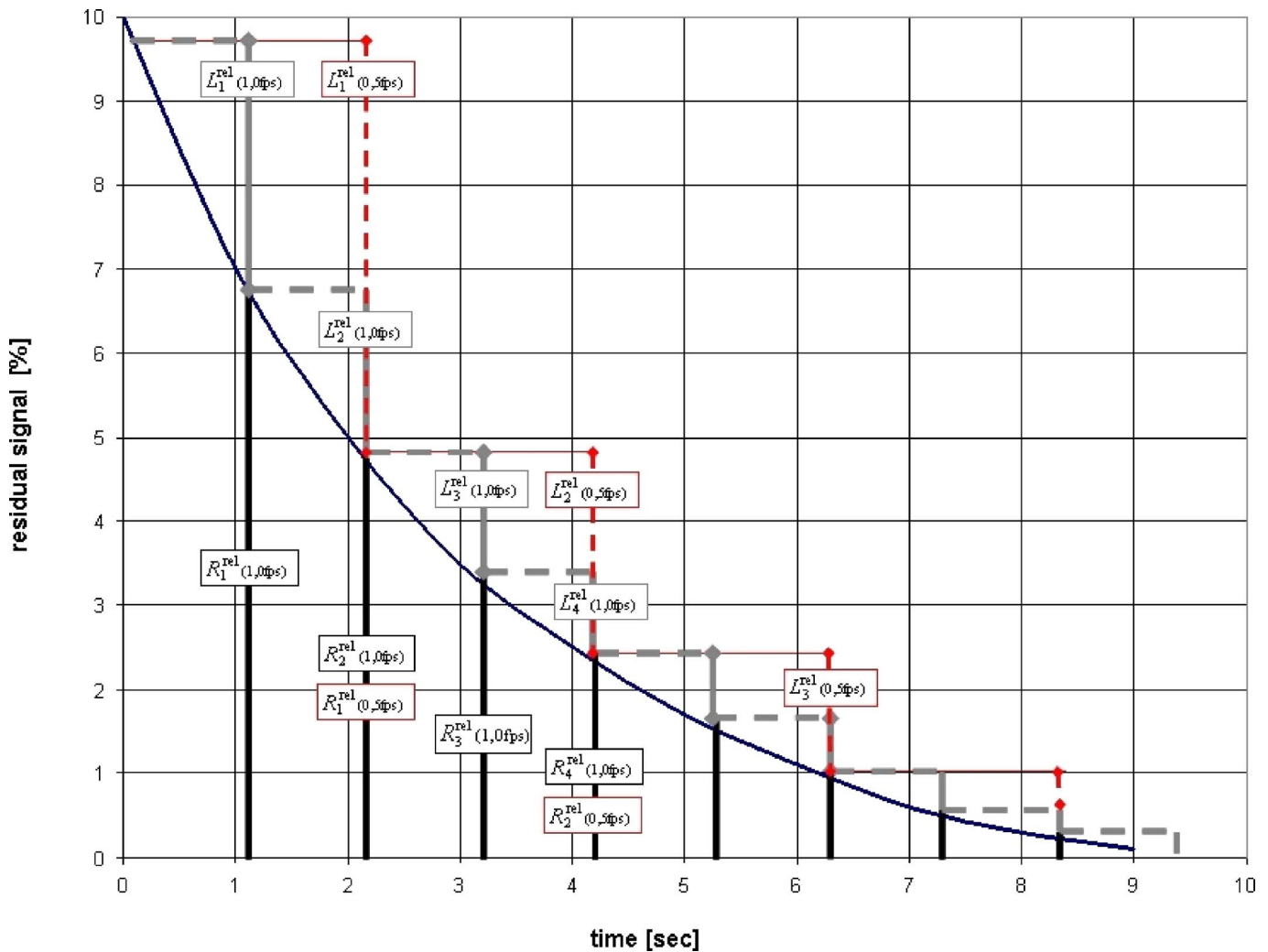


FIG. 5. The lag effect: Correlation between time dependent decay curve and relative lag values.

ing the amount of the remaining signal) is calculated by accumulation of the global mean values of the remaining N_0 images:

$$L^{\text{abs}} = \sum_{n=1}^{N_0} \frac{\omega/\gamma I_n}{G}. \quad (14)$$

N_0 represents maximum possible order of lag correction as well. After normalization the relative lag values for each order n are given by

$$L_n^{\text{rel}} = \frac{\omega/\gamma I_n}{L^{\text{abs}}}, \quad n = 1, \dots, N_0. \quad (15)$$

The normalized decay curve dependent on the image number can be written as

$$R_n^{\text{rel}} = 1 - \sum_{i=1}^n L_i^{\text{rel}}, \quad n \in \{1, \dots, N_0\}. \quad (16)$$

As the frame rate f is known, R_n^{rel} represents the residual signal at a certain time $t=n/f$ in percentage of the total lag. Therefore, a time dependent curve, the decay curve, can be fitted through the measured data point (e.g., multiexponential fit). With the help of this decay curve the relative lag values for any frame rate can be estimated. Figure 5 illustrates how the relative lag values can be derived for a different frame rate.

A complete dataset for lag correction includes all relative mean values $L_n^{\text{rel}}(f)$ for the designated frame rate f that are higher than 1.0%.

II.E.6. Calibration step 4: Delta detector calibration

The acquisition mode for CBCT (orbital or angular rotation) requires a delta calibration. Again, a valid or updated offset map set $\check{\Omega}$ is necessary. For reasons of noise reduction typically 2–3 white field image sequences ($W_{s,n}^X$) for high and low gain, acquired at half saturation dose each (dose index $d=4$, $d=12$, respectively) during an orbital rotation of the C arm, are averaged:

$${}^d_M W_n^X(u,v) = \frac{1}{S} \cdot \sum_{s=1}^S {}^d W_{s,n}^X(u,v). \quad (17)$$

The corresponding gain map (dose index $d=4$, $d=12$, respectively) of the multipoint gain calibration is selected. A delta map ${}^r\Delta^X$ for high and low gain is created for every rotation angle of the C arm rotation $r \in \{0^\circ, \dots, 200^\circ\}$ in the following way:

$${}^r\Delta^X(u,v) = \frac{{}^d_M \Gamma^X(u,v)}{{}^d_M W_n^X(u,v) - {}_M \Omega^X(u,v)}, \quad (18)$$

$$n = 1, \dots, N; \quad r = \frac{n}{M} \cdot 200^\circ.$$

A complete dataset for delta correction includes 200 delta maps (one per orbital angle r) for each gain ($X \in \{H, L\}$). Each map indicates the change in the exposure distribution

over the detector surface in comparison to the reference position ($r=0^\circ$).

II.E.7. Summary

Recapitulating, three kinds of calibration maps (gain, delta, temperature maps) and a set of relative lag values were generated during the offline calibration process (see Fig. 3). These data plus an additional contemporary offset map set are the sources for the (online) correction of a raw image sequence.

II.F. Online correction

The activity diagram of a complete online correction procedure is shown in Fig. 4. Basically, it can be separated into five steps: The offset correction, eliminating the pixel individual offset, the delta correction, considering the dynamic changes of the pixel individual sensitivity, the temperature correction, providing valid gain maps for the current temperature, the multipoint gain calibration, normalizing the pixel individual response over the complete dynamic range and the lag correction, removing ghost images due to afterglow and signal retention in the panel.

Steps one to four have to be done for each gain individually and can be summarized as sensitivity calibration, while step five is done on the already combined images and considers the temporal dependencies. The source is always a raw image sequence. For dual gain mode the raw image sequence has to be separated into high and low gain sequences. Except for lag compensation, all correction steps run parallel for high and low gain.

II.F.1. Correction step 1: Offset correction

For offset correction of the raw image sequence I_n^X with N images (e.g., $N=400$ for a 3D soft tissue scan) a valid offset map is necessary. As the offset is correlated to the temperature, the offset map has to be updated, if the temperature changes significantly (e.g., 2°C) In practice the offset map is permanently updated, if the detector is in stand-by mode. The correction is done through a pixel-by-pixel subtraction of the offset map mean values (${}_M \Omega^X$):

$$\omega I_n^X(u,v) = I_n^X(u,v) - {}_M \Omega^X(u,v), \quad n = 1, \dots, N. \quad (19)$$

II.F.2. Correction step 2: Delta correction

For delta correction each image is weighted pixel by pixel with the corresponding delta map that is linked to the appropriate orbital angle r :

$$\omega/\delta I_n^X(u,v) = \omega I_n^X(u,v) \cdot {}^r\Delta^X(u,v),$$

$$n = 1, \dots, N; \quad r = 0^\circ, \dots, 200^\circ; \quad r = \frac{n}{N} \cdot 200^\circ. \quad (20)$$

If the number of images N is higher than 200, a linear interpolation of the neighboring delta maps is possible.

II.F.3. Correction step 3: Temperature correction

The temperature correction is not a correction of the images themselves, but an adaptation of the multipoint calibration gain maps (${}^d_M\Gamma^X$) for the current temperature. First the adequate temperature map ${}^{t_0}\Theta^X$ for current temperature $t_0 \in \{t_B, \dots, t_E\}$ has to be selected from the temperature map archive. This is done by a comparison of the contemporary offset map mean matrix ${}_M\Omega^X$ with the stored offset map mean matrices of the temperature calibration process (${}^t_M\Omega^X$). The best matching offset map can be assigned for example through a pixel-by-pixel summation of the absolute variations. The offset map (mean value map) with the smallest total variation ${}^{t_0}\mathbf{V}$ is selected:

$${}^{t_0}\mathbf{V} = \min \left\{ \sum_{u,v} |{}_M\Omega^X(u,v) - {}^t_M\Omega^X(u,v)| \right\}_{t \in \{t_B, \dots, t_E\}}. \quad (21)$$

The temperature map linked to the assigned offset map of the archive is selected:

$${}^{t_0}_M\Omega^X(u,v) \Leftrightarrow {}^{t_0}\Theta^X(u,v). \quad (22)$$

The mean value matrices of all gain maps for the multipoint calibration, are weighted with this temperature map:

$$\begin{aligned} {}^{d,t_0}_M\tilde{\Gamma}^X(u,v) &= {}^{d,t_E}_M\tilde{\Gamma}^X(u,v) \cdot {}^{t_0}\Theta^X(u,v) \\ d &= 1, \dots, 14. \end{aligned} \quad (23)$$

II.F.4. Correction step 4: Multipoint gain correction

Now the images can be corrected with the temperature adjusted gain maps. For each pixel signal S of the offset and delta corrected image ${}^{\omega/\delta}I_n^X$ two gain maps are identified: The one with the next possible higher signal S_+ and the one with the next possible lower signal S_- at the position (u, v) . With the help of the original (nontemperature corrected) global mean value of each gain map (${}_G\Gamma_-^X, {}_G\Gamma_+^X$), two gain factors are computed. A linear interpolation is done depending on the relation of the three signals S, S_+, S_- to calculate a signal dependent scalar gain factor $g_n^X(u, v, S)$:

$$g_n^X(u, v, S) = \left(\frac{S - S_-}{S_+ - S_-} \right) \cdot \frac{{}_G\Gamma_+^X}{S_+} + \left(\frac{S_+ - S}{S_+ - S_-} \right) \cdot \frac{{}_G\Gamma_-^X}{S_-},$$

$$S = {}^{\omega/\delta}I_n^X(u, v); \quad S_- = {}_M\tilde{\Gamma}_-^X(u, v); \quad S_+ = {}_M\tilde{\Gamma}_+^X(u, v),$$

$${}_G\Gamma_-^X = \frac{1}{u_0 v_0} \sum_{u,v} {}_M\tilde{\Gamma}_-^X(u, v); \quad {}_G\Gamma_+^X = \frac{1}{u_0 v_0} \sum_{u,v} {}_M\tilde{\Gamma}_+^X(u, v). \quad (24)$$

For multipoint gain correction the offset and delta corrected raw images are multiplied pixel by pixel with the signal dependent gain factor $g_n^X(u, v, S)$:

$${}^{\omega/\delta/\partial/\gamma}I_n^X(u, v) = {}^{\omega/\delta}I_n^X(u, v) \cdot g_n^X(u, v, S). \quad (25)$$

So far this is done both for high and low gain image separately. As a next step both gain images have to be combined to one single image with extended dynamic range.

II.F.5. Combination of high and low gain image (part of step 4 for DGR mode)

As all pixels have the same exposure response after the previous correction steps, the combination can be done by using the different global mean values of the appropriate gain maps. The high gain signal stays unchanged while the low gain signal is multiplied by the ratio of averaged high gain global mean and averaged low gain global mean of the neighbor's gain maps:

$$\begin{aligned} &{}^{\omega/\delta/\partial/\gamma}I_n^H(u, v); \\ &{}^{\omega/\delta/\partial/\gamma}I_n^L(u, v) = {}^{\omega/\delta/\partial/\gamma}I_n^L(u, v) \cdot \frac{{}_G\Gamma_-^H + {}_G\Gamma_+^H}{{}_G\Gamma_-^L + {}_G\Gamma_+^L}. \end{aligned} \quad (26)$$

Theoretically three different cases for pixel combination can occur:

(1) Both (high and low gain) pixel values are valid. The resulting pixel signal is computed by averaging

$$\begin{aligned} C_n(u, v) &= {}^{\omega/\delta/\partial/\gamma}I_n(u, v) \\ &= ({}^{\omega/\delta/\partial/\gamma}I_n^H(u, v) + {}^{\omega/\delta/\partial/\gamma}I_n^L(u, v))/2. \end{aligned} \quad (27)$$

(2) The high gain pixel value is saturated (e.g., areas of direct radiation or object borders). Its information cannot be used for combination. The resulting pixel signal is represented by the low gain pixel value only:

$$C_n(u, v) = {}^{\omega/\delta/\partial/\gamma}I_n(u, v) = {}^{\omega/\delta/\partial/\gamma}I_n^L(u, v). \quad (28)$$

(3) The low gain pixel value falls below a certain threshold, where additional quantization noise has an influence on SNR performance. This can happen behind thick or highly absorbing objects. The low gain information should not be used for combination in this case. The resulting pixel signal is represented by the high gain pixel value only:

$$C_n(u, v) = {}^{\omega/\delta/\partial/\gamma}I_n(u, v) = {}^{\omega/\delta/\partial/\gamma}I_n^H(u, v). \quad (29)$$

In practice, additional linear interpolations at both crossover sections are applied.

II.F.6. Defect pixel detection and correction (part of step 4)

While combining both gain images defects are estimated with help of the recent offset map $\hat{\Omega}$ and the gain maps ${}^d\hat{\Gamma}$ of the multipoint calibration archive: Pixel values beyond certain threshold borders for the mean ${}_M\Omega^X$ or standard deviation ${}_{SD}\Omega^X$ of the offset map are marked in a binary defect map. Particularly defective lines or columns are conspicuous in their offset behavior and can therefore be easily detected. As the offset map is regularly updated, recently failed pixel or lines are considered as well.

Besides the offset, a pixel can be defective because of its gain behavior. Again the mean value $\mu_M \Gamma^X$ and standard deviation map $\sigma_{SD} \Gamma^X$ of the gain maps are analyzed, and pixels with bad behavior are also marked in the binary defect map. A gain defect can be, for example, highly nonlinear signal response, bad SNR performance, or early saturation. The correction of defects can be done by bilinear interpolation of the nearest neighbor responses. In the simplest case a 3×3 median filter can be used as well. This correction is sufficient, if at least four of the nearest neighbors in a 3×3 kernel are valid. According to the detector specification a maximum of five defective pixels (crossing of defective line and column) in a 3×3 neighborhood is allowed. The remaining defective pixels can be interpolated by using the median filter again. A more detailed description of the different methods for defect pixel detection is not within the scope of this article.

II.F.7. Correction step 5: Lag correction

The lag compensation is done on the corrected image sequence $C_n(u, v)$. A lag corrected image $\tilde{C}_n(u, v)$ is calculated using the history of in practice $K=10$ previous images with the corresponding relative lag values L_k^{rel} (relative amount of residual signal from image $n-k$ in the current image n , $k=1, \dots, K$) for each pixel (u, v) :

$$\tilde{C}_n(u, v) = C_n(u, v) \cdot \frac{1}{1 + \sum_{k=1}^K L_k^{\text{rel}}} - \sum_{k=1}^K L_k^{\text{rel}} \cdot \tilde{C}_{n-k}(u, v). \quad (30)$$

While the first term increases the signal for the amount of total lag that is currently trapped, the second term takes the remaining lag signals from previous images into consideration.

As this algorithm is based on recursive subtraction, the first image of the sequence has to be free of lag. Only in this case the second summand is zero, and the first image can be corrected. This requirement is fulfilled if the time between the acquisitions of two sequences is long in relation to the decay curve of the detector. In practice, this is the case if no images are acquired for 2 min.

II.F.8. Summary

In comparison to the conventional method for detector calibration [see Eq. (1)] the new calibration model provides several new and improved correction steps [see Eqs. (19), (20), (23), and (25)–(30)] that are necessary to consider all major dependencies of the individual pixel sensitivity for 2D and 3D imaging. In the following, the results of the new model as well as the achievable improvements in image quality will be discussed.

III. RESULTS AND DISCUSSION

III.A. Dual gain readout mode

Three different approaches exist to implement the combination of two different gain modes (high/low gain) to extend the global dynamic range.¹⁰

The simplest method is to read the image twice, once for low and once for high gain, and combine these images to one image with extended dynamic range. This can be achieved by a reread of the same line without resting inbetween. But on the one hand, it necessitates a doubling of the image numbers and, on the other hand, cuts in half the possible frame rate. An additional disadvantage is that the standard correlated double sampling (SCDS, see Ref. 11) is only valid for one gain (e.g., high) and therefore increases the noise for the other gain (e.g., low).

A second approach lets the detector automatically decide which gain mode is appropriate. This mode is also called dynamic gain switching. The frame rate and data handling stay unchanged. In theory, this would be the best solution, but in practice calibration is difficult, because the switch between the different gains leads to major artifacts within the crossover section. A calibration of this mode seems to be very complex, if maximum image quality is required (e.g., 3D soft tissue imaging). Additionally, SCDS is also only valid for one mode.

The third DGR mode corresponds to the one described in the calibration model. It is a trade off between the first and second mode. Data lines are read out alternately, one in high gain and one in low gain. Due to split readout design and starting with low gain lines, the two lines in the middle of the plate are high gain lines. This readout scheme causes a reduction of the frame rate by a factor two and an increase of the raw data by a factor two in comparison to 2×2 binned single gain mode, that has a dimension of 1024×768 pixel. But it provides the best possible SNR for both gains because SCDS is done for each mode separately. The object information that can be seen in both gain images can be combined and the clipped information (normally object border) of the high gain image can be replaced by the information of the low gain (extension of the dynamic range, see Fig. 2). Especially for 3D imaging, this is a major benefit, because artifacts due to saturation at the object borders are eliminated.

III.B. Temperature correction

The offset correction does not differ from the conventional offset correction method (subtraction of the averaged pixel individual offset signal).^{14,16,17} But the offset map is additionally used for the temperature effect correction. This can only be done because the PaxScan 4030CB provides an analog offset compensation by standard correlated double sampling (SCDS).¹¹ Besides reduction of the reset kTC noise (switching noise) of the charge amplifier and the $1/f$ noise [noise contribution whose power spectra $P(f)$ as a function of the frequency f behaves like: $P(f) = 1/f$] generated in subsequent circuits, it cancels the drift in the offset voltage of signal processing circuits. Therefore, only the offset effects

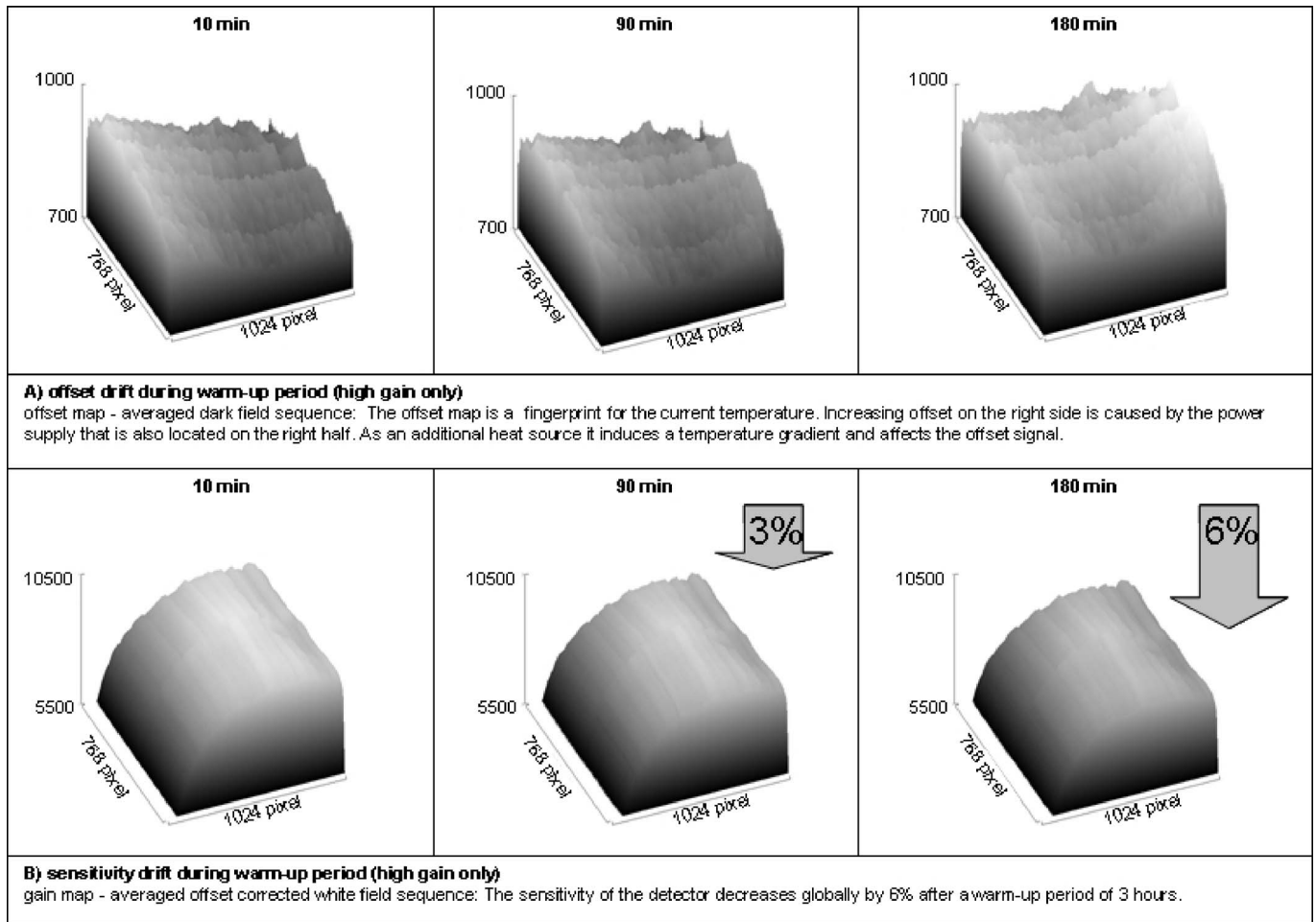


FIG. 6. Temperature dependencies of pixel offset and sensitivity for the high gain.

generated in the pixel itself persist. These pixel offset effects are strongly correlated with temperature, so a current offset map can be used as a fingerprint for the effective temperature. The offset changes during warm up period for high gain are shown in Fig. 6. Also the corresponding drift of the pixel individual sensitivity of the high gain is shown. This drift behavior results in three different artifacts for 2D and 3D imaging respectively (see Table VII).

With an adequate offset map archive and the linked temperature map archive, a valid temperature map for current temperature can be estimated, and a valid gain map can be computed. This model can also be expanded to a multipoint calibration because the temperature map is supposed to be valid for every gain map for first order approximation. With valid gain maps these additional artifacts can be well suppressed.

TABLE VII. Temperature dependent artifacts in 2D images and 3D slices.

2D artifact	3D artifact
Horizontal brightness gradient	Radial brightness gradient
Virtual shift of the intensity	HU shift
Additional streak artifacts	Additional ring artifacts

III.C. Multipoint gain correction

As the signal response of each individual pixel is not exactly linear over the complete dynamic range a single gain map cannot ensure artifact free 2D projection images. A real flat field image can be achieved only if the image dose is equivalent to the calibration dose. That is why a signal dependent gain factor is necessary for each individual pixel. If this dependency is estimated by a polynomial fit¹⁷ for each individual pixel, the flexibility for a later temperature or delta correction is lost. That is why the multipoint calibration is done with the help of the original gain maps and a linear interpolation within the relevant supporting points.

Figure 7 shows the differences between a single point and a multipoint calibrated image sequences in two dimensions. The stripe artifacts of the 2D projection images cause ring artifacts within the reconstructed 3D volume (see Fig. 12 below and compare Sec. IV). With additional multipoint gain correction these artifacts disappear.

III.D. Delta correction

As the gain correction equalizes inhomogeneous illumination as well, the combination of temperature correction and multi-point gain calibration ensures the best possible image

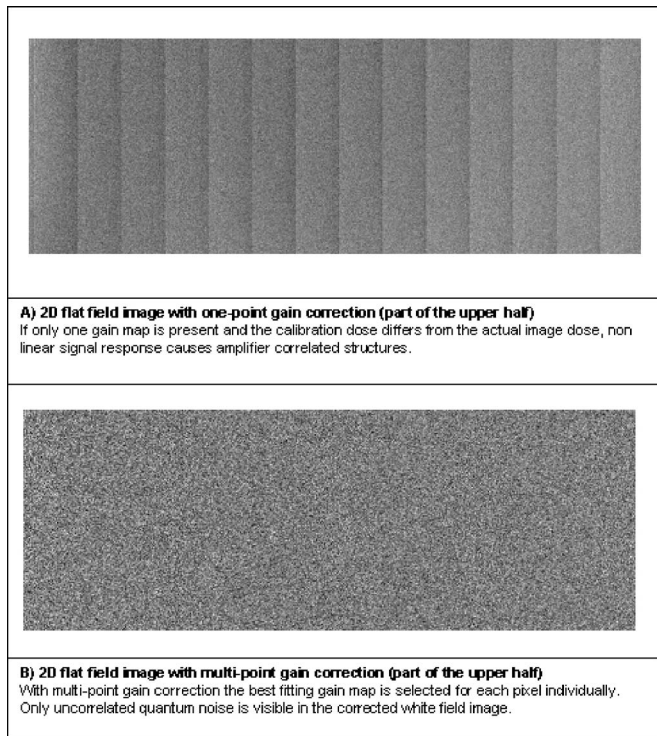


FIG. 7. Multipoint gain correction: Benefit on 2D flat field projection images.

quality only if the radiation geometry stays unchanged. If, for example, source-to-detector distance changes or the central beam shifts, artifacts may appear at positions with high sensitivity gradient. For mobile *C* arms the latter is the case during an orbital rotation for CBCT.¹ Figure 8 shows the movement of the illumination and the effects on the cali-

brated projection images. Usually these effects were compensated with a rather high, smoothed weighting matrix. Therefore, only global variations of the brightness are corrected and pixel individual effects are neglected.

As a new concept, the delta correction is implemented. It is a pixel-by-pixel correction matrix that takes care of all changes (deltas) in the pixel sensitivity, regardless of the cause (changing the radiation geometry, detector aging, see Figs. 8 and 9). The most important advantage of such a delta concept is very obvious: As this correction consists of all changes in the pixel individual sensitivity, it is the only recalibration step that is necessary. A complete temperature and multipoint correction would be very complex and time consuming. For example, the temperature calibration itself would take at least as long as the warm-up period (up to 4 h; see Section III B). Additionally, several white field images have to be acquired to compute the gain maps (see Section III C).

As an example for CBCT with a mobile *C* arm, averaging of 2–3 orbital scans without object for delta maps generation is sufficient to obtain the correction factors which when applied to images restores image quality. Figure 10 shows the different artifacts that can occur if the basic calibration is obsolete. In this case the multi-point gain calibration was performed 10 months before the flat field image acquisition. With an up to date delta calibration, artifacts are suppressed and the image quality is similar to a recently established basic calibrated system.

III.E. Lag correction

The lag effect within an image sequence as described by Siewerdsen *et al.*¹² can be significantly reduced by the recur-

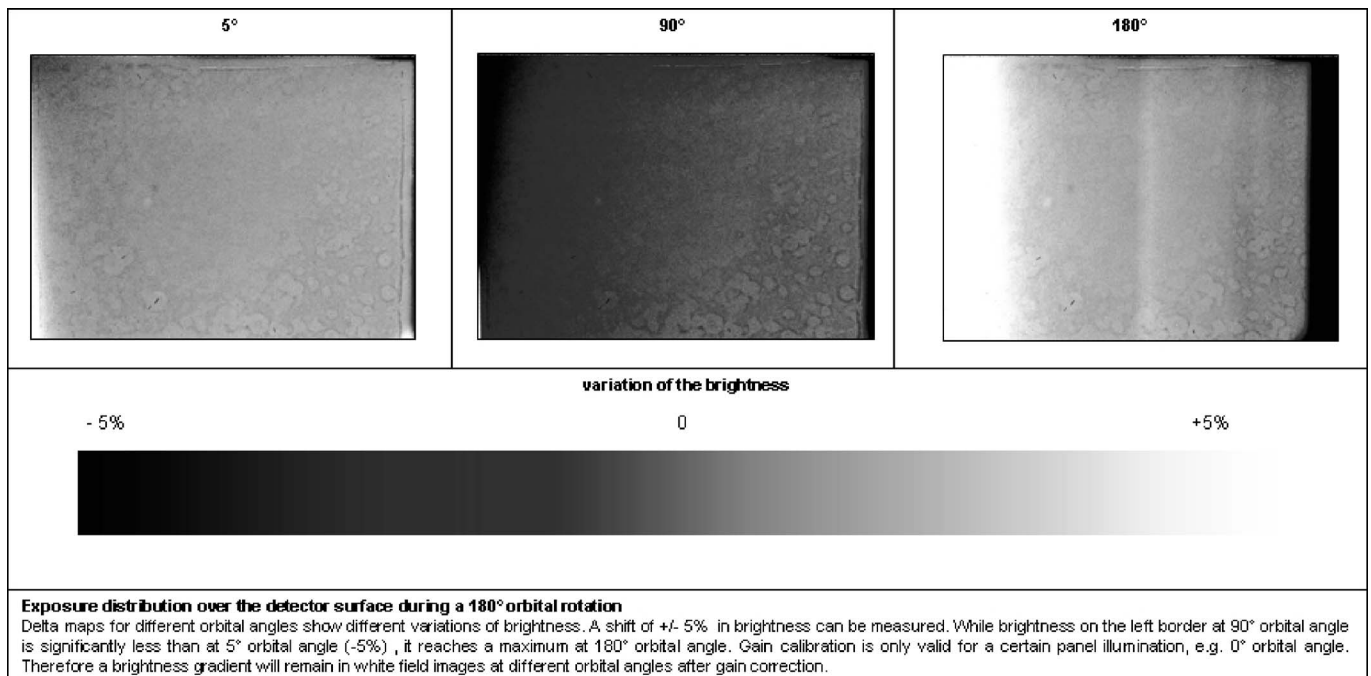


FIG. 8. Exposure distribution over the detector surface during 180° orbital rotation.

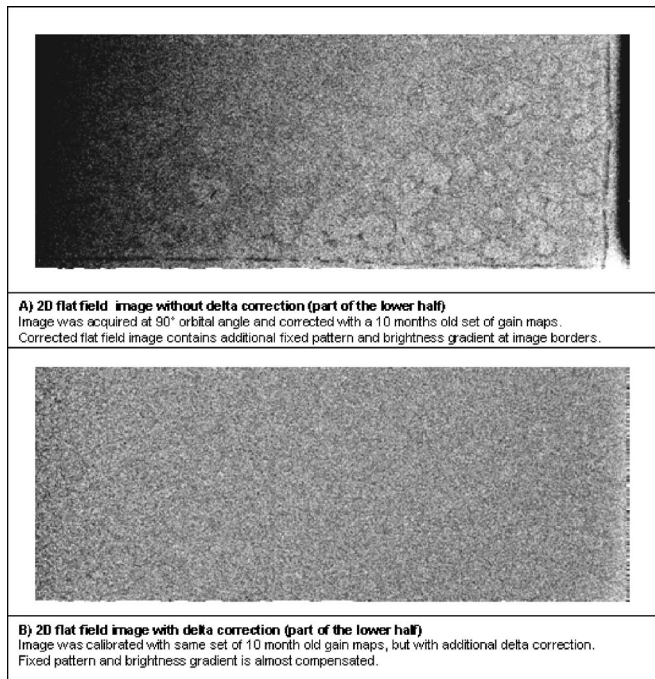


FIG. 9. Delta correction: Benefit on 2D flat field projection images.

sive subtraction algorithm. Figure 11 gives a demonstration of a 2D image sequence with and without lag compensation. In the special case of a rotationally symmetric phantom, the shadow balls within the 2D projection image sequence result in comet balls in the 3D reconstruction. This artifact was already described by Siewerdsen *et al.*¹³ After lag compensation these comet balls disappear (see Fig. 11). In general (nonrotational symmetric object), the lag effect causes blur-

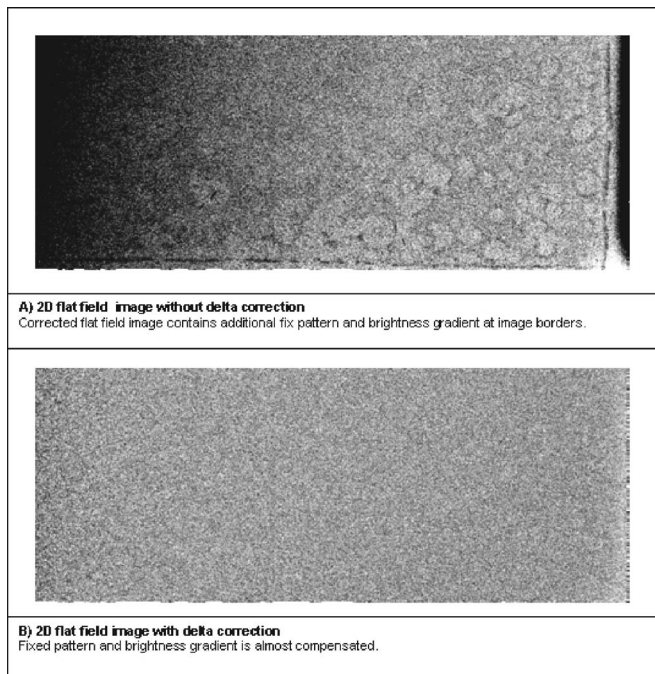


FIG. 10. Delta correction: Effect on 2D flat field projection images.

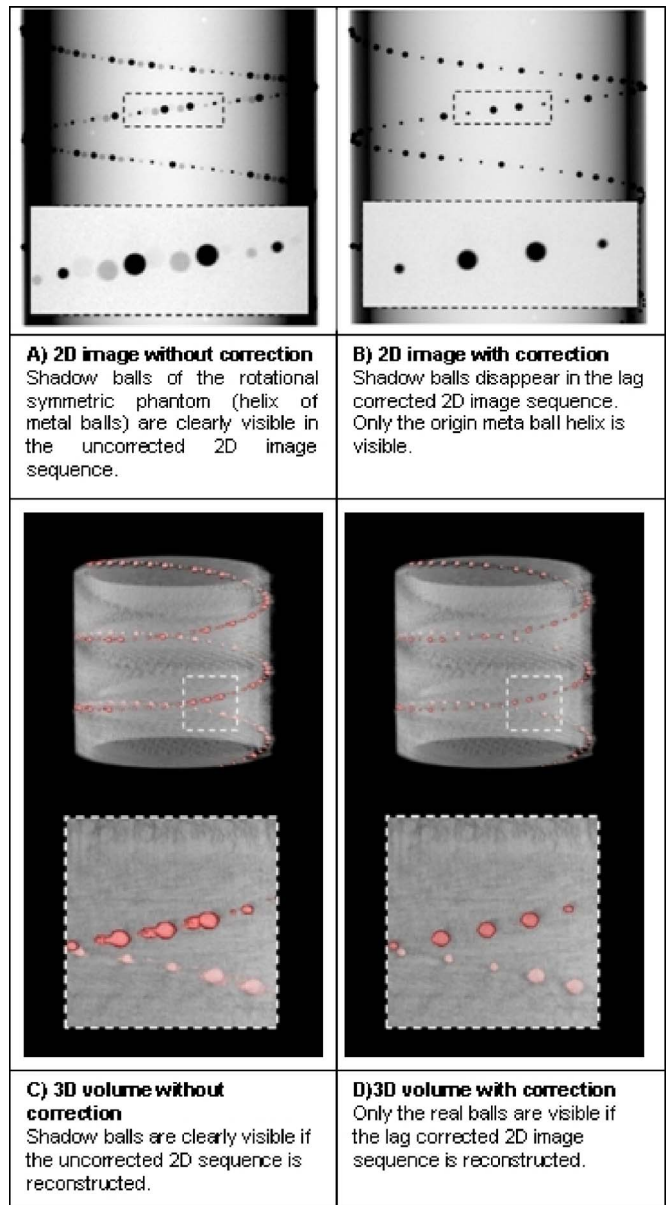


FIG. 11. Effect of image lag for a rotational symmetric phantom.

ring in the 3D volume and reduces the spatial resolution. As the lag effect could be significantly reduced from detector generation to detector generation,¹¹ it is less a problem for image quality at CBCT as for switching from low gain to high gain modes (switching artifacts) in 2D imaging. This happens when structures caused by the lag effect in a high dose imaging mode are amplified and become visible, if the sensitivity changes after a mode switch to low dose imaging.

IV. CONCLUSION

The described calibration model for a dual gain flat panel detector considers major effects and dependencies that can occur at CBCT with mobile C arm systems, and simultaneously minimizes the effort for recalibration. Figure 12 gives an example with state-of-the-art corrections [see Fig. 12(a)] and with corrections based on the new calibration

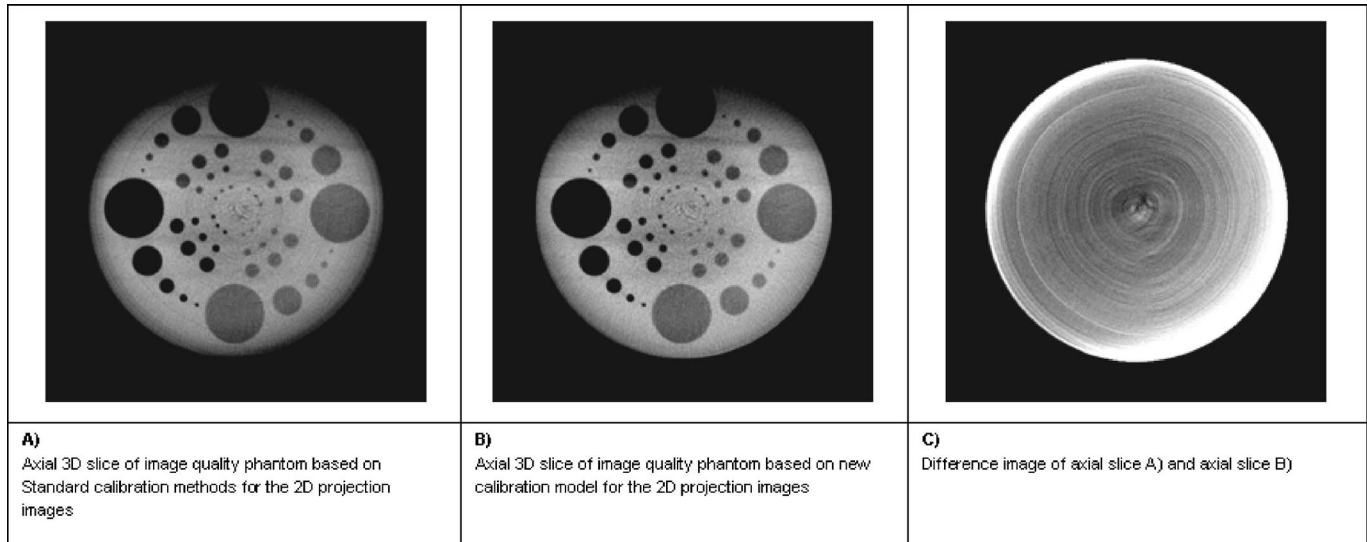


FIG. 12. 3D Image quality based on standard calibration method and new calibration model

model [see Fig. 12(b)]. In this case a 3D quality phantom was scanned immediately after switching on the flat detector. With standard methods three remaining artifacts can be observed that were caused by insufficient detector calibration:

- (1) The nonlinear signal response respective to the complete dynamic range causes ring artifacts in the axial 3D slices. With additional multi-point gain correction these artifacts can be well compensated.
- (2) The temperature dependency of the sensitivity causes additional ring artifacts in the axial 3D slices and a global shift of the reconstructed density values. For a temperature change between 22 °C after switch on and 50 °C after warm-up period a shift of about 20 HU (Hounsfield units) was measured. With additional temperature correction both artifacts can be suppressed well.
- (3) Variations of the beam geometry during the orbital rotation cause a brightness gradient toward the borders of the reconstruction volume. The edges of the phantom appear oblate. With delta correction this artifact can be reduced because variations in the illumination are compensated in each projection image

(It should be noted, that the remaining brightness gradient in top/bottom direction is caused by insufficient compensation of oversampled data starting at 180° minus cone angle. This effect can be compensated by an algorithm introduced by Parker.¹⁸⁾)

The disparity of the correction methods becomes clearly visible in the difference image. The new calibration model contributes to increasing the image quality and reducing the artifact level for cone beam CT significantly. The concept of basic (multipoint gain, lag, and temperature) and delta calibration also contains promise for the implementation in future C arm products. Not all offline calibration steps are real time relevant. Multipoint gain and lag calibration can be automated and performed in approximately 20 min (depending on the number of gain steps). Temperature calibration lasts

until steady-state temperature is reached. This depends on the detector and can be up to 4 h. But these steps have to be done only once. Only the delta calibration has to be repeated in regular intervals (approximately three months, similar to regular gain recalibration) and can be performed in a couple of minutes. Prototype implementation shows that all online corrections steps can be done in real time with current image processing platforms and hardware technology.

For reasons of completeness, it should be mentioned that additional effects can influence the sensitivity of each individual pixel. Among them is, for example, spectral nonlinearity, meaning that beam hardening caused by the examined object or x-ray scattering changes the x-ray spectrum. The calibration is valid, strictly speaking, only for a certain x-ray spectrum. Another effect is a long persistent ghosting artifact due to bright burning (radiation induced gain change) that cannot completely be covered by the lag correction. In the case of CBCT with a mobile C arm, which was the motivation for this model, these effects are not supposed to be dominant and can therefore be neglected. But this assumption has to be proven by further investigations.

^{a1)}Author to whom correspondence should be addressed. Electronic mail: christian.schmidgunst.ext@siemens.com

¹D. Ritter, J. Orman, C. Schmidgunst, and R. Graumann, "3D soft tissue imaging with a mobile C-arm," *Comput. Med. Imaging Graph.* **31**, 91–102 (2007).

²P. Pohlentz, M. Blessmann, L. Oesterhelweg, C. R. Hebermann, P. Bege-mann, C. Schmidgunst, F. Blake, D. Schulze, Klaus Püschel, R. Schmelzle, and M. Heiland, "3D C-arm as an alternative modality to CT in postmortem imaging: Technical feasibility," *Forensic Sci. Int.*, PMID: 17640838 (2007).

³P. Pohlentz, M. Blessmann, L. Oesterhelweg, C. Braun, C. Schmidgunst, D. Schulze, K. Püschel, and M. Heiland, "Dreidimensionale forensische Bildgebung mithilfe eines neuen C-Bogens," *Rechtsmedizin* **17**, 35–39 (2007).

⁴S. Hirota, N. Nakao, S. Yamamoto, K. Kobayashi, H. Maeda, R. Ishikura, K. Miura, K. Sakamoto, K. Ueda, and R. Baba, "Cone beam CT with flat-panel detector digital angiography system: Early experience in abdominal interventional procedures," *Cardiovasc. Intervent Radiol.* **29**, 1034–1038 (2006).

- ⁵K. Nikolau, T. Flohr, and K. Stierstorfer, "Flat panel computed tomography of human *ex vivo* heart and bone specimens: Initial experience," *Eur. Radiol.* **15**, 329–333 (2005).
- ⁶J. H. Siewerdsen, D. J. Moseley, S. Burch, K. Bisland, A. Bogaards, B. C. Wilson, and D. A. Jaffray, "Volume CT with a flat-panel detector on a mobile, isocentric C-arm: Pre-clinical investigation and guidance of minimally invasive surgery," *Med. Phys.* **32**, 241–254 (2005).
- ⁷J. A. Rowlands and J. Yorkston, "Flat panel detectors for digital radiography," in *Handbook of Medical Imaging* (SPIE, Bellingham, 2000), pp. 223–328.
- ⁸R. E. Colbeth, M. J. Allen, and D. J. Day, "Flat-panel imaging system for fluoroscopy applications," *Proc. SPIE* **3336**, 376–387 (1998).
- ⁹R. E. Colbeth, S. Boyce, and R. Fong, "40 × 30 cm flat panel imager for angiography, R&F and cone-beam CT applications," *Proc. SPIE* **4320**, 84–102 (2001).
- ¹⁰Evangelos Matsinos and Wolfgang Kaissl, "The dual-gain mode: a way to enhance the dynamic range of X-ray detectors," arXiv.org:physics/0607021 (2006).
- ¹¹P. G. Roos, R. E. Colbeth, I. Mollov, P. Munro, J. Pavkovich, E. J. Seppi, E. G. Shapiro, C. A. Tognina, G. F. Virshup, J. M. Yu, and G. Zentai, "Multiple-gain-ranging readout method to extend the dynamic range of amorphous silicon flat-panel imagers," *Proc. SPIE* **5368**, 139–149 (2004).
- ¹²J. H. Siewerdsen and D. A. Jaffray, "A ghost story: spatio-temporal response characteristic of an indirect-detection flat-panel imager," *Med. Phys.* **26**, 1624–1641 (1994).
- ¹³J. H. Siewerdsen and D. A. Jaffray, "Cone-beam computed tomography with a flat-panel imager: Effects of image lag," *Med. Phys.* **26**, 2635–2647 (1999).
- ¹⁴J. P. Moy and B. Bosset, "How does real offset and gain correction affect the DQE in images from X-ray flat detector?" *Proc. SPIE* **3569**, 90–97 (1999).
- ¹⁵D. Zhang, R. Ning, B. Chen, and D. L. Conover, "Accurate and efficient calibration method for a selenium flat-panel detector-based volume tomographic angiography imaging system," *Proc. SPIE* **3659**, 626–634 (1999).
- ¹⁶J. A. Seibert, J. M. Boone, and K. K. Lindfors, "Flat-field correction technique for digital detectors," *Proc. SPIE* **3636**, 348–354 (1998).
- ¹⁷A. L. C. Kwan and J. A. Seibert, "An improved method for flat-field correction of flat panel X-ray detector," *Med. Phys.* **33**, 391–393 (2006).
- ¹⁸D. L. Parker, "Optimal short scan convolution for fanbeam CT," *Med. Phys.* **9**, 254–257 (1982).